Optics Letters

Wide-field optical coherence microscopy of the mouse brain slice

Eunjung Min,[1] Junwon Lee,[1] Andrey Vavilin,[1] Sunwoo Jung,[1,2] Sungwon Shin,[1,2] Jeehyun Kim,[3] and Woonggyu Jung[1,2,*]

[1]Department of Biomedical Engineering, Ulsan National Institute of Science and Technology (UNIST), Ulsan, South Korea
[2]Center for Soft and Living Matter, Institute for Basic Science (IBS), Ulsan, South Korea
[3]School of Electronics Engineering, Kyungpook National University, Daegu, South Korea
*Corresponding author: wgjung@unist.ac.kr

The imaging capability of optical coherence microscopy (OCM) has great potential to be used in neuroscience research because it is able to visualize anatomic features of brain tissue without labeling or external contrast agents. However, the field of view of OCM is still narrow, which dilutes the strength of OCM and limits its application. In this study, we present fully automated wide-field OCM for mosaic imaging of sliced mouse brains. A total of 308 segmented OCM images were acquired, stitched, and reconstructed as an *en-face* brain image after intensive imaging processing. The overall imaging area was 11.2×7.0 mm (horizontal × vertical), and the corresponding pixel resolution was 1.2×1.2 μm. OCM images were compared to traditional histology stained with Nissl and Luxol fast blue (LFB). In particular, the orientation of the fibers was analyzed and quantified in wide-field OCM. © 2015 Optical Society of America
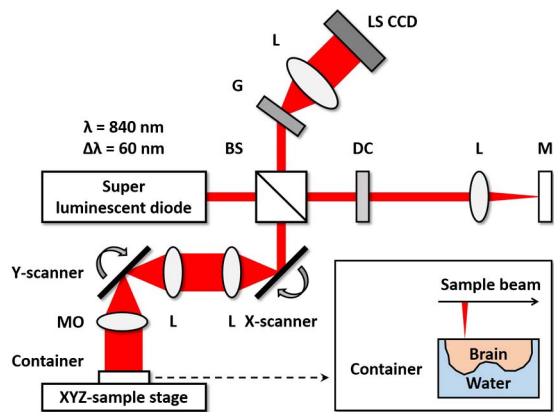
Brain structure has been visualized by various imaging modalities that can provide essential keys to understanding the brain's functions and dysfunctions. Brain imaging modalities such as MRI and CT are able to visualize the whole brain, but are less able to recognize cyto- and myelo-architecture in tissue because of the inherent limitations of spatial resolution. Thus, they have been complemented with the traditional histology for identifying and confirming micro-structures of the brain. However, the whole procedure of histology (e.g., formalin-fixation, dehydration, paraffin embedding, staining, and sectioning) is quite time-consuming and labor intensive, and generally provides only localized morphologies. Furthermore, it is readily damaged in the process of micro-thin sectioning, and the outcome of the histological section is fairly varied by hands-on skills and the experience of users.

To compensate for the drawbacks of traditional histology, optical coherence microscopy (OCM) has been introduced as an alternative tool because it has unique advantages in providing label-free, noninvasive, and cross-sectional tissue structure with micro-level resolution [1]. OCM has been widely researched for visualizing single myelin fiber [2], cerebral cortex [3], tumorous tissue [4], laminar structure of isocortex [5], and neuronal cell bodies in the brain [6,7]. Whereas most OCM systems provide the regional geometric anatomy with narrow field of view, so it has restriction to derive important information such as the microscopic feature of myelin and their overall connectivity [8]. Here, we introduce wide-field OCM to perform multi-scale analysis of mouse brain slices covering the micro-scale (biological component, e.g., cell bodies and myelin fiber), as well as the meso-scale (geometric anatomy). The acquired OCM images of several regions were compared with the gold standard histologies.

Figure 1 shows the schematic of a spectral domain OCM system, which was developed in this study. A superluminescent light emitting diode (Superlum, D-849-HP) with a center wavelength of 840 nm and a spectral bandwidth of 60 nm was used as the light source, which provides a 4 μm axial resolution in air. The light was launched and divided into two optical paths at the beam splitter: one delivering to the sample and the other going to the reference arm. In sample path, we used 20× and 40× objective offering lateral resolutions of 1.3 and 0.7 μm in air, respectively. Reflected lights from each path return to the beam splitter and were combined and detected by a spectrometer that consists of a grating (Wasatch Photonics, 1200 lines/mm), focusing lens, and line-scan CCD (Basler, spl2048–140 km). The signal acquired from the spectrometer was processed by fast Fourier transform (FFT) and converted to a log intensity profile that indicates depth information (A-line) [9]. A-lines were accumulated as x and y scanners navigated the specimens, and, finally, 2D and 3D OCT images were produced. The sensitivity of the OCT system was 92.8 dB.

For the preparation of brain slices, four-week-old ICR mice were transcardially perfused with 30 ml PBS before dissecting to eliminate blood inside the brain. The animal procedure was approved by the In Vivo Research Center and carried out in
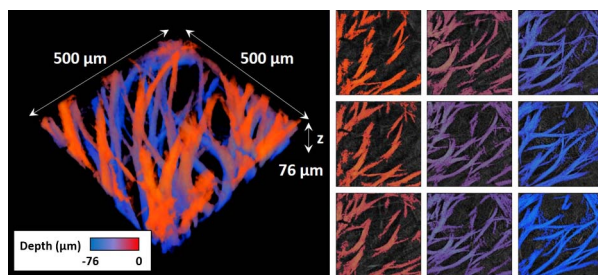
Fig. 1. Schematics of wide-field optical coherence microscopy. BS, beam splitter; DC, dispersion compensation unit; G, grating; L, lens; LS CCD, line-scan charge-coupled device camera (2048 pixels, 12 bits); M, mirror; MO, microscope objective.

Fig. 3. Mosaic image processing algorithm. Each tile of mosaic image was aligned and merged after local and global intensity correction.

accordance with Institutional Animal Care and Use Committee standards. During image acquisition, the brain was kept inside a container to flatten the non-uniform surface of brain tissue and to prevent its dehydration.
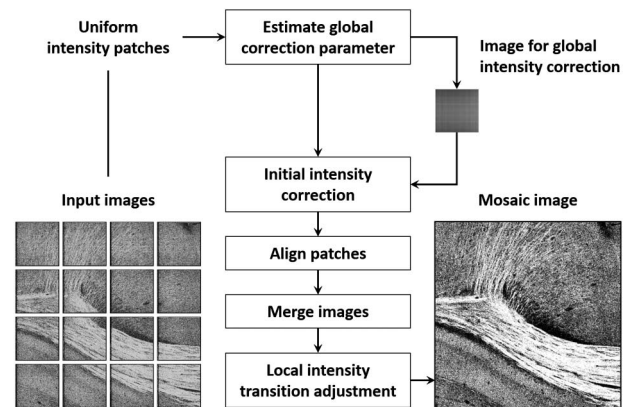
In this study, a total 308 OCM images set from the coronal section brain was acquired by 20× microscope objective (Olympus, UPLSAPO20X). To achieve the wide-field OCM image, sliced brain tissue was mounted on the three-axis motorized stages and imaged by the mosaic technique. Whenever single OCM volume data were acquired, the motorized stage moved the sample to the next programmed position to cover the entire brain slice. This process was fully automated and controlled by Labview software. The field of view of a single mosaic image set was 625 × 625 μm overlapping 20% with adjacent images. The image acquisition time for single image set consisting of 500 B-scans was 25 s.

Figure 2 shows one of the representative image sets of 3D myelin fibers in the caudate putamen region. OCM shows good contrast in the myelin fibers, and identifies the distribution and orientation of each fiber without a contrast agent or any labeling process. However, it still has a limitation in that this technique rules out looking at the morphological characteristics of myelin fibers because of the narrow field of view.

To achieve the wide-field OCM image, all OCM image sets were stitched and reconstructed as a single *en-face* image. Since it requires intensive image processing, home-built software was specifically developed for this study. Image reconstruction involves several processing steps as shown in Fig. 3. First, the input images have global intensity distribution that is originated from lens aberration in common. Input images with high mean intensity and low intensity variance were analyzed to perform global intensity correction. Then, we subtract this image from each image, which reduced the effect of nonuniform intensity distribution. After initial intensity correction, images were aligned by scanning order of the motorized stages. Lastly, sharp transitions between neighboring images were post-processed to increase its contrast. The whole process was automatically performed and total computational time of image processing regarding to 308 images set was about 2 h.

The size of the reconstructed image was 11.2 × 7.0 mm (horizontal × vertical) which covers the entire coronal area of

Fig. 4. Comparison of OCM (a) and Nissl-LFB stained images (b) of mouse brain. Red arrows indicated in the Nissl-LFB image show tissue damage caused by thin sectioning and over-staining. Several regions in (a) and (b) are enlarged on the right side. cc, corpus callosum; HPF, hippocampus formation; CP, Caudoputamen; cpd, cerebral peduncle. The size of each of the enlarged images is 1 × 1 mm (four-segmented image) and the pixel resolution is 1.2 × 1.2 μm.
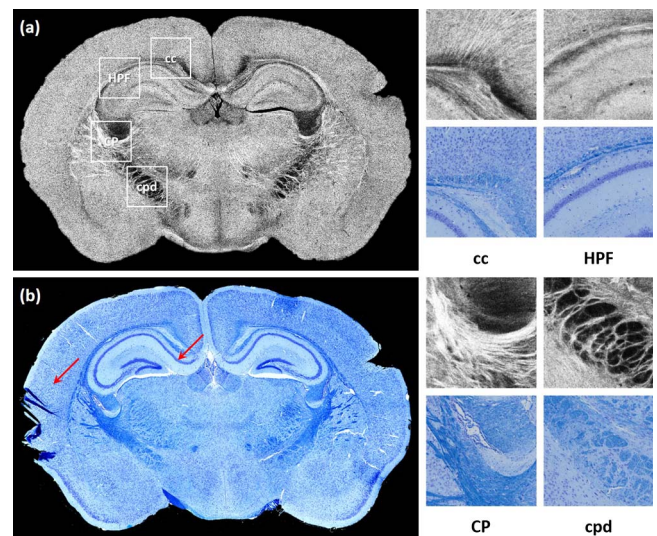

Fig. 2. Volumetric image of myelin fiber bundle in the caudoputamen of a mouse brain. The *en-face* image of myelin fiber with respect to depth is presented aside, and the depth is encoded as color.

sliced brain tissue as depicted in Fig. 4(a). For the comparison study with conventional histology, brain tissue was stained with Nissl-Luxol fast blue (LFB) immediately after OCM imaging. Nissl-LFB labels specifically in cell body and myelin sheath. Our result shows that the morphology of brain tissue between OCM and the stained histological section has a strong correlation. In particular, OCM images have even better contrast for the fiber bundles in the region of the corpus callosum (cc), caudo-putamen (CP), and cerebral peduncle (cpd) because light scattering in the lipids of myelin fiber are relatively stronger than the surrounding tissue [10]. One of the strong advantages of wide-field OCM imaging is the simple preparation of brain tissue and noninvasive imaging capability. It enables us to avoid the routinely occurring issues seen in histological sectioning, such as over-staining and tissue damage, as indicated with red arrows in Fig. 4(b). Considering these results, wide-field OCM is competitive tool over the conventional histology and has potential to observe the multiple brain slices.

Our research also involves finding the orientation of fibers in brain tissue. There are several mathematical algorithms used to estimate the orientation of fiber tracts in medical imaging. In this study, Radon transform (RT) was specifically utilized because it minimizes artifacts and extracts accurate orientation values. To extract the orientation angle of myelin fiber, several analysis processes are required [11].

Figure 5 describes the analysis process of extracting the orientation angles of myelin fiber in the white matter of a mouse brain. To begin with, we chose the region of interest in the white matter as shown in Fig. 5(a). The short space Fourier transform (SSFT) written in Eq. (1) was then performed to analyze localized regions as depicted in Figs. 5(b) and 5(c). A Gaussian window filter $g(x, y)$ was used for localization of the signal which is also referred to as 2D spatial Gabor transform (GT). The variables f_x and f_y are spatial frequencies in the frequency domain, corresponding to spatial variables x and y. x_0 and y_0 are at the center of the window filter in the spatial domain. σ is the standard deviation of the Gaussian function along x and y, and $I(x, y)$ denotes the image in the spatial domain. However, the localization creates an uncertainty problem

between space and frequency resolution. Based on the Gabor uncertainty principle, it can be written as $\sigma_x \sigma_f \geq 1/4\pi$. Hence, the size of the Gaussian filter was selected, depending on the region of the brain and the texture of the myelin fibers therein. In here, σ_x and σ_f were set as 30 μm and 2.6/mm, respectively, and the sweep interval of the filter was 30 μm. As the next step, the result obtained from GT was Radon transformed by Eq. (2). This process gave us the orientation angle of the spatial frequency. f'_x and f'_y are the spatial frequency variables in the new coordinate after the coordinate system tilted by angle θ. The result of its RT is described in terms of f'_x and θ, as described in Fig. 5(d). Then, predominant orientation value was extracted with the line of $f'_x = 0$ which gives the same value when it is measured clockwise from the vertical line in Fig. 5(c). However, the orientation value was obtained only where the fiber is isotropic. In our case, we determined the isotropic when the average value of normalized intensity $\frac{1}{N} \sum_{i=1}^{N} I(\theta_i)/I_{\max}$ is smaller than the threshold of 0.3. By repeating the steps of Figs. 5(b)–5(d), a map of orientation angle Fig. 5(e) was obtained:
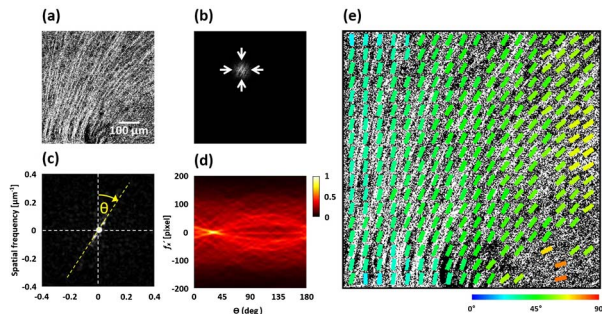
$$G(x, y, f_x, f_y) = \int_{-\infty}^{\infty} \int_{-\infty}^{\infty} g(x, y) I(x, y) \mathrm{d}x \mathrm{d}y,$$
$$g(x, y) = (1/2\pi\sigma^2) e^{-0.5/\sigma^2 [(x-x_0)^2 + (y-y_0)^2]} e^{-i2\pi[f_x x + f_y y]},$$
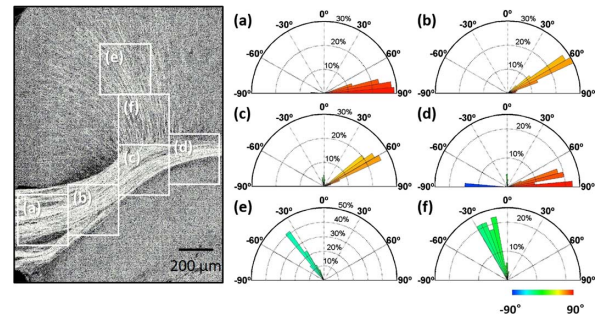$$\tag{1}$$

$$R_\theta(f'_x) = \int_{-\infty}^{\infty} G(f'_x, f'_y) \mathrm{d}f'_y$$
$$(f'_x, f'_y) = (f_x \cos\theta - f_y \sin\theta, f_x \sin\theta + f_y \cos\theta). \tag{2}$$

By using this algorithm, the orientation of myelin fiber along the corpus callosum and singular cortex was statistically analyzed, as presented in Fig. 6. OCM images were acquired by 40× microscope objective (Olympus, LUMPLFLN20XW) for better identification of the fibers where pixel resolution is 0.6×0.6 μm. The size of the overall image and white box are 1.3×1.5 mm and 0.3×0.3 mm (horizontal × vertical), respectively. We analyzed the six areas of (a)–(f) in the left-hand figure using the algorithm in Fig. 5 that represents fiber tracts in the brain. In this calculation, window size and sweep interval

Fig. 5. Image processing to extract the orientation angle of myelin fiber in white matter of a mouse brain. To start with, we chose the region of interest in white matter (a) and swept the image with a Gaussian filter to calculate the orientation angle at a localized region (b). By applying Fourier transform for the selected region (b), a signal was separated by spatial frequency (c). Radon transform with 1° resolution was then applied (d). The orientation angle was extracted from the intensity profile of $f'_x = 0$ in (d). The processes of (b)–(d) are repeated for the overall region of the image. As a result, a map of orientation angles can be obtained (e).

Fig. 6. Orientation of fiber bundles in the corpus callosum and singular cortex using wide-field OCM. Each of the figures (a)–(f) is quantitatively analyzed with circular histograms (a)–(f) on the right. The radial axis indicates percentage of number of data with respect to orientation angle. By comparing (a)–(d) and (e)–(f) groups, the orientation angle abruptly changes because the corpus callosum and singular cortex have different myelo-architectures.

were 12 and 6 µm, respectively. Therefore, circular histograms for orientation corresponding to Figs. 6(a)–6(f) were obtained. They present the percentage of number of data (radial axis) with respect to orientation angle. The figure shows different orientation characteristics for different regions of the brain. The myelin fiber in the corpus callosum is dominantly aligned close to a horizontal line. On the other hand, in the singular cortex, the orientation suddenly changes to the vertical line. It is similar to diffusion tensor imaging, but with high resolution.

In this study, we developed wide-field OCM which can provide comprehensive morphologies of mouse brain slices in *en-face* view. It clearly visualized hippocampus, corpus callosum, cortex, and so on. OCM images using endogenous contrast showed a strong correlation with traditional histology. In this comparison study, we found that OCM contrast is better at delineating fiber tracts in brain tissue. For further study of the fiber tracking, the polarization sensitive OCT is worth to be considered because the fiber tract is sensitive birefringent material [12]. Wide-field OCM images also enable us to analyze the orientation of fibers, which typical OCM, having a narrow field of view, is unable to do. Our system has been utilized to reconstruct single brain slices, but can be applied to multiple slices for the volumetric visualization of the brain. Thus, a platform of wide-field OCM is a very promising tool for use in neuroscience research, and is particularly well suited for systematic studies of brain anatomy for the understanding of mouse models of various cognitive disorders.

REFERENCES

1. D. Huang, E. A. Swanson, C. P. Lin, J. S. Schuman, W. G. Stinson, W. Chang, M. R. Hee, T. Flotte, K. Gregory, C. A. Puliafito, and J. G. Fujimoto, Science **254**, 1178 (1991).
2. J. B. Arous, J. Binding, J. Léger, M. Casado, P. Topilko, S. Gigan, A. C. Boccara, and L. Bourdieu, J. Biomed. Opt. **16**, 116012 (2011).
3. V. J. Srinivasan, H. Radhakrishnan, J. Y. Jiang, S. Barry, and A. E. Cable, Opt. Express **20**, 2220 (2012).
4. O. Assayag, K. Grieve, B. Devaux, F. Harms, J. Pallud, F. Chretien, C. Boccara, and P. Varlet, Neuroimage Clin. **2**, 549 (2013).
5. C. Magnain, J. C. Augustinack, M. Reuter, C. Wachinger, M. P. Frosch, T. Ragan, T. Akkin, V. J. Wedeen, D. A. Boas, and B. Fischl, Neuroimage **84**, 524 (2014).
6. F. Li, Y. Song, A. Dryer, W. Cogguillo, Y. Berdichevsky, and C. Zhou, Neurophotonics **1**, 025002 (2014).
7. C. Magnain, J. C. Augustinack, E. Konukoglu, M. P. Frosch, S. Sakadžić, A. Varjabedian, N. Garcia, V. J. Wedeen, D. A. Boas, and B. Fischl, Neurophotonics **2**, 015004 (2015).
8. C. J. Goergen, H. Radhakrishnan, S. Sakadžić, E. T. Mandeville, E. H. Lo, D. E. Sosnovik, and V. J. Srinivasan, Opt. Lett. **37**, 3882 (2012).
9. G. Häusler and M. W. Lindner, J. Biomed. Opt. **3**, 21 (1998).
10. C. Leahy, H. Radhakrishnan, and V. J. Srinivasan, Biomed. Opt. Express **4**, 1978 (2013).
11. Y. Mega, M. Robitaille, R. Zareian, J. McLean, J. Ruberti, and C. DiMarzio, Opt. Lett. **37**, 3312 (2012).
12. H. Wang, J. Zhu, and T. Akkin, Neuroimage **84**, 1007 (2014).